International Journal of Multiphase Flow 35 (2009) 738–746

Contents lists available at ScienceDirect

International Journal of Multiphase Flow

journal homepage: www.elsevier.com/locate/ijmulflow

A long gas bubble moving in a tube with flowing liquid

James Q. Feng *

Cardiovascular R & D, Boston Scientific Corporation, Three Scimed Place C-150, Maple Grove, MN 55311, USA

ARTICLE INFO

Article history:
Received 28 October 2008
Received in revised form 31 March 2009
Accepted 31 March 2009
Available online 10 April 2009

Keywords:
Long bubble
Flow in tube
Finite-element computation

ABSTRACT

The steady axisymmetric behavior of a long gas bubble moving with a flowing liquid in a straight round tube is studied by computationally solving the nonlinear Navier–Stokes equations using a Galerkin finite-element method with a boundary-fitted mesh for wide ranges of capillary number *Ca* and Reynolds number *Re*. As illustrated with a series of computed results, the hydrodynamic stresses due to liquid flow around the bubble tend to shape the middle section of long bubbles into a cylinder of constant radius, with a uniform annular liquid flow adjacent to the tube wall. But the surface tension effect tends to cause nonuniformities in the annular liquid film thickness. The annular liquid film thickness generally increases with increasing *Ca*, but decreases with increasing *Re*. In units of the bubble velocity relative to the tube wall, the average liquid flow velocity $\overline{U}$ is always less than unity, indicating that the bubble always moves faster than the average liquid flow. For convenient practical applications, a least-square fitted empirical formula is obtained in a form of $\overline{U} = 1 - \widetilde{A}/(1 + \widetilde{B}\,Ca^{-\widetilde{C}})$ with $\widetilde{A}, \widetilde{B}$, and $\widetilde{C}$ being functions of *Re*. The fact that the behavior of long bubbles moving in a tube appears independent of the bubble length is consistent with the inconsequential influence of the uniform annular film flow in bubble's middle section to the bubble dynamics. Whereas all the long bubbles exhibit similar nose profile, various tail shapes can be obtained by adjusting the values of *Re* and *Ca*.

1. Introduction

In a tube, the motion of a gas bubble relative to the tube wall can occur in the presence of the buoyancy force due to gravitational field or when the surrounding liquid flows in response to a pressure gradient through the tube. The buoyancy-driven motion of a gas bubble through viscous liquid in a (vertical) round tube was studied by numerous authors and extended in a recent computational work of Feng (2008). The present work focuses on the steady axisymmetric motion of a long bubble with viscous liquid flowing in a straight round tube, excluding the buoyancy effect. Here a long bubble should be regarded as a bubble with its basic fluid mechanical behavior, such as its velocity (relative to the tube wall), nose and tail shapes, etc., becoming independent of the bubble volume.[1] Different bubble behavior is expected between the buoyancy-driven motion and that due to the pressure-gradient-driven liquid flow, because the background liquid flow fields differ considerably. This problem is of interest not only for the sake of understanding the fundamental fluid mechanics, but also in practical applications such as multiphase flow in the micro-gravity environment as well as in situations where the velocity of the flowing liquid is much greater than that due to the buoyancy-driven motion or when the buoyancy effect becomes negligible.

The motion of long bubbles in round tubes due to flowing liquids was studied by Fairbrother and Stubbs (1935), who found that the bubble moves faster than the average speed of liquid flow by an amount that can be determined by the square root of capillary number. The maximum value of capillary number for the formula of Fairbrother and Stubbs to be valid was shown by Taylor (1961) to be about an order of magnitude greater than that of the upper limit of Fairbrother and Stubbs' experiments. Taylor (1961) also pointed out that the ratio of bubble speed versus the average speed of liquid flow approaches an asymptotic value at large capillary number. The asymptotic value suggested by Taylor (1961) was further refined with experimental measurements by Cox (1962) who also presented a theoretical analysis in the limit of large capillary number. For long bubbles in the low-speed limit, Bretherton (1961) was able to determine the liquid film thickness from the local flow field around the bubble nose, using a lubrication flow theory with matched asymptotic expansion for the transition region between the uniform liquid film and spherical bubble nose. Later, Bretherton's analysis was refined by Park and Homsy (1984) and extended to larger capillary number by Ratulowski and Chang (1989) who computed isolated bubbles and bubble trains moving in circular and square tubes. By experimentation, Goldsmith and Mason (1963) established the evidence that the

* Tel.: +1 763 255 0265; fax: +1 763 255 0499.
E-mail address: james.feng@bsci.com

[1] For buoyancy-driven long bubbles, also known as Taylor bubbles, the bubble's volume-equivalent radius is typically greater than that of the tube, although some smaller bubbles may also exhibit similar long bubble behavior Feng (2008).

0301-9322/$ - see front matter © 2009 Elsevier Ltd. All rights reserved.
doi:10.1016/j.ijmultiphaseflow.2009.03.012

annular liquid film between the bubble nose and bubble tail has a uniform thickness wherein the liquid is at rest with respect to the tube wall. More general theoretical studies of thin liquid films (associated with long bubbles) were carried out by Teletzke (1983), Teletzke et al. (1987) and Teletzke et al. (1988) who generalized the Bretherton's (1961) theory to account for the effects of intermolecular forces in terms of disjoining pressure in submicroscopically thin films, surface-active impurities, etc. with the lubrication flow theory. Further experimental measurements of the liquid film thickness left behind after the passage of a long bubble in a round tube were carried out by Schwartz et al. (1986) with lubrication flow analysis of the annular film stability.

Equivalent to considering the leading meniscus of a long bubble moving with a liquid flow through the tube, the displacement of viscous liquid by a semi-infinite bubble in a tube was computed with a finite difference method by Reinelt and Saffman (1985) and with a finite-element method by Shen and Udell (1985) in the creeping flow regime. The boundary integral analysis of Martinez and Udell (1989) yielded results in very good agreement with the published experimental data, though it was restricted to the creeping flow of (very) long bubbles in round tubes with leading meniscus and trailing meniscus computed separately, assuming the leading and trailing menisci being connected by an annular film of constant thickness at rest with respect to the tube wall. A finite-element method for computing free surface flows with the free surface parametrized by means of spines (following that described by Kistler and Scriven (1983)) was used by Giavedoni and Saita (1997) to study both the axisymmetric and 2D (planar) cases of a gas finger (or semi-infinite bubble) steadily displacing a Newtonian liquid, revealing the types of recirculating flow patterns ahead of the bubble nose as envisaged by Taylor (1961). The fluid inertia effect studied by Giavedoni and Saita (1997) for the displacement of viscous liquid by a semi-infinite bubble in a 2D channel was further extended by Heil (2001), showing a sequence of closed vortices (or "cat's eye" pattern) appears in the recirculating flow ahead of the bubble nose at finite Reynolds number. Computations of entire bubbles moving with flowing liquid in a round tube seem to be lacking in the literature, especially for bubbles with significant free-surface deformations.

In the present work, numerical solutions are computed for cases of long bubbles in relatively small tube, in a problem domain enclosing the entire bubble. A Galerkin finite-element method with full Newton iterations is used for simultaneously solving the steady axisymmetric Navier–Stokes equations together with the elliptic mesh-generation equations for accurately tracking the entire bubble surface deformations Christodoulou and Scriven (1992) and de Santos (1991).[2]

2. Mathematical formulation and computational method

As in Feng (2008), the problem of a gas bubble moving with a liquid of constant density ρ, viscosity μ, and surface tension γ in a round tube is described in terms of dimensionless parameters and variables with length measured in units of the tube radius R, velocity $\boldsymbol{v}$ in units of bubble's velocity U relative to the tube wall, and pressure p in units of $\mu U/R$. A reference frame moving with the bubble is adopted here with the coordinate origin fixed at the bubble's centroid. With the hydrodynamic stresses due to the flow of gas inside the bubble being ignored, the axisymmetric, laminar liquid flow around the bubble is governed by the steady incompressible Navier–Stokes equation system

$$\frac{1}{2}Re\,\boldsymbol{v}\cdot\nabla\boldsymbol{v}=\nabla\cdot\boldsymbol{T}\quad\text{with}\quad\boldsymbol{T}\equiv-p\boldsymbol{I}+\nabla\boldsymbol{v}+(\nabla\boldsymbol{v})^{T}\tag{1}$$

and

$$\nabla\cdot\boldsymbol{v}=0,\tag{2}$$

where the Re denotes the Reynolds number defined as $2\rho UR/\mu$, $\boldsymbol{I}$ the identity tensor, and superscript 'T' stands for the transpose.

A cylindrical (z,r)-coordinate system is used with the z-axis coinciding with the axis of symmetry (i.e., the centerline of the tube) and pointing in the same direction as the wall velocity relative to the bubble. Thus, at the bubble surface conservation of momentum is satisfied by imposing the traction boundary condition

$$\boldsymbol{n}\cdot\boldsymbol{T}=\frac{1}{Ca}\left[\frac{d\boldsymbol{t}}{ds}+\frac{\boldsymbol{n}}{r}\frac{dz}{ds}\right]-p_a\boldsymbol{n}\quad\text{on }S_f,\tag{3}$$

where $Ca\equiv\mu U/\gamma$ is the capillary number, the local unit normal vector $\boldsymbol{n}$ at the free surface points from the liquid into gas, the local unit tangent vector $\boldsymbol{t}$ points in the direction of increasing s along the boundary and relates to $\boldsymbol{n}$ in such a way that $\boldsymbol{n}\times\boldsymbol{t}=\boldsymbol{e}_\theta$ (with the right-handed coordinate system (z,r,θ) used in the present work). The uniform excess pressure inside the bubble p_a is solved as an unknown to satisfy an overall constraint that the volume enclosed by the free surface S_f does not vary

$$\int_{S_f}r^2\frac{dz}{ds}\,ds=\frac{4}{3}R_b^3=\frac{\text{volume}}{\pi},\tag{4}$$

where R_b denotes the volume-equivalent radius of the bubble.[3] Another overall constraint that the bubble's centroid remains at the coordinate origin

$$\int_{S_f}zr^2\frac{dz}{ds}\,ds=0.\tag{5}$$

is satisfied by solving for the value of p_i at the inlet boundary (e.g., $z=-6$ in Fig. 1) with the boundary condition

$$v_r=0\text{ and }\boldsymbol{e_z}\boldsymbol{e_z}:\boldsymbol{T}=-p_i\quad\text{on }S_{\text{inlet}}.\tag{6}$$

Moreover, the flow velocity field must satisfy

$$\boldsymbol{n}\cdot\boldsymbol{v}=0\quad\text{on }S_f\text{ and }r=0,\tag{7}$$

at the free surface S_f, due to the kinematic condition, and at the axis of symmetry $(r=0)$, as required by the symmetry condition. In addition, the stress-free symmetric condition at the axis of symmetry $(r=0)$ can be expressed as

$$\boldsymbol{e_z}\boldsymbol{e_r}:\boldsymbol{T}=0\quad\text{at}\quad r=0,\tag{8}$$

where $\boldsymbol{e_z}$ and $\boldsymbol{e_r}$ denote the unit vectors in the z- and r-directions, respectively.

At the tube wall $(r=1)$, the Dirichlet type of condition for constant (relative) flow velocity is imposed, i.e.,

$$\boldsymbol{v}=\boldsymbol{e_z}\quad\text{on}\quad r=1.\tag{9}$$

At the downstream (or 'outflow') boundary (e.g., $z=10$ of Fig. 1), fully-developed flow condition for hydrodynamic stresses is used, i.e.,

$$\boldsymbol{e_z}\boldsymbol{e_r}:\boldsymbol{T}=\frac{\partial v_z}{\partial r}\text{ and }\boldsymbol{e_z}\boldsymbol{e_z}:\boldsymbol{T}=0\quad\text{on }S_{outlet}.\tag{10}$$

As illustrated by Feng (2007, 2008), solutions of the present problem can be computed by discretizing the partial differential equa-

[2] The computational software used here is the same one as that described in Feng (2007, 2008), with more details given at the website http://james.q.feng.googlepages.com/FECAWwelcome.html.

[3] As commented by Feng (2008), it seems to be more meaningful to discuss the bubble size in terms of bubble volume rather than of bubble (volume-equivalent) radius R_b for long bubbles in relatively small tubes.

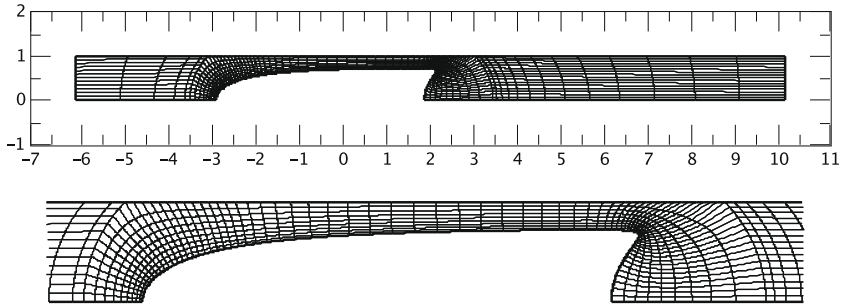

Fig. 1. Finite-element mesh of the problem domain for a bubble of volume $= 2\pi$ (as exemplified by the case of $Re = 100$ and $Ca = 1$). The locations of inlet and outlet boundaries are verified to be far enough that the changes in computed results presented here are numerically negligible with moving S_{inlet} and/or S_{outlet} further away.

tion system (1)–(10) with the Galerkin method of weighted residuals using finite-element basis functions (Strang and Fix, 1973). In doing so, the problem domain is divided into a set of quadrilateral elements (cf. Fig. 1), with biquadratic basis functions being used for expanding the velocity field and linear discontinuous basis function for pressure. The positions of finite-element mesh nodes around the deformable bubble surface are determined by a pair of elliptic partial differential equations that are also be descretized by the Galerkin finite-element method (Christodoulou and Scriven, 1992; de Santos, 1991). Then, the set of nonlinear algebraic equations of Galerkin's weighted residuals is simultaneously solved by Newton's method of iterations (Ortega and Rheinoldt, 1970). At each Newton iteration, the Jacobian matrix of sensitivities of residuals to unknowns is evaluated with the values of unknowns determined in the previous iteration. The resulting linear algebra system is then solved by direct factorization of the Jacobian matrix with a modified version of Hood's frontal solver (Hood, 1976). The iteration is continued until the L_2 norm of residual vector becomes less than 10^{-8}.

With the present mathematical formulation, the Reynolds number Re and capillary number Ca are the two independent parameters can be conveniently specified. The value of p_i in (6) is solved as part of the solution, becoming another independent parameter associated with the mathematical system. But the value of p_i depends on the locations of the inlet and outlet boundaries; therefore it does not easily connect to a practically measurable quantity. As the direct consequence of p_i, the average liquid flow velocity (relative to the tube wall),

$$\overline{U} \equiv 2\int_0^1 (1 - v_z)\, r\, dr \quad \text{on } S_{\text{inlet}} \quad (\text{or } S_{\text{outlet}}), \tag{11}$$

relates to the (constant) liquid flow rate in the tube independent of the location of inlet and outlet boundaries.[4] Hence, $\overline{U}$ instead of p_i is used in the present work as an independent parameter describing the driving mechanism for the bubble motion (relative to the tube wall). Once Re, Ca, and $\overline{U}$ are given, other relevant dimensionless parameters associated with a solution can all be calculated in terms of them. For example, the Weber number $We \equiv 2\rho U^2 R/\gamma$ can be expressed as $Re\,Ca$. Because of the nondimensional form of governing equations adopted in the present work, each solution corresponding to a set of specified Re, Ca, and $\overline{U}$ can represent numerous seemingly different fluid systems and tube sizes by virtue of dynamical similarity (Batchelor, 1967).

[4] Due to the imposed pressure difference between inlet and outlet boundaries $-p_i$, the flow velocity at the inlet boundary becomes a superposition of a Poiseuille flow and a uniform flow at the bubble speed (because the reference frame here is chosen to move with the bubble).

3. Solutions for long bubbles moving with flowing liquids

With the availability of many published data and formulas for the case of long bubbles at $Re = 0$, a comparison of the present computational results with previous ones should be an interesting first exercise. At $Re = 0$ and $Ca = 0.001$, the computed values of $\overline{U}$ are, respectively, 0.97531 and 0.97526 for bubbles of volume = 2π and 3π, in reasonable agreement with Bretherton's theory (1961) for $Ca \leqslant 5 \times 10^{-3}$,

$$\overline{U} = 1 - 1.29\,(3\,Ca)^{2/3}, \tag{12}$$

which predicts the value of $\overline{U}$ equal to 0.97345 at $Ca = 0.001$. For $10^{-3} \leqslant Ca \leqslant 10^{-2}$, Fairbrother and Stubbs (1935) obtained an empirical correlation formula that corresponds to

$$\overline{U} = 1 - \sqrt{Ca}, \tag{13}$$

predicting 0.9684 (as comparable to the computed value 0.9753), 0.9000, and 0.6838 for $Ca = 0.001$, 0.01, and 0.1, respectively. The present computations yield the values of $\overline{U}$ for $Ca = 0.01$ and 0.1, respectively, 0.8976 (0.8967) and 0.6944 (0.6945) for bubbles of volume = $3\pi(= 2\pi)$ at $Re = 0$, validating (13) up to $Ca = 0.1$ as did Taylor (1961) experimentally.

Based on the assumption that the liquid in a uniform annular liquid film is at rest with respect to the tube wall (an evidence experimentally established by Goldsmith and Mason (1963)), conservation of mass leads to (cf. Fairbrother and Stubbs, 1935)

$$\hat{r}^2 = \overline{U}, \tag{14}$$

where $\hat{r}$ denotes the theoretical value of radial coordinate of the annular film free surface with uniform thickness. Based on results of (13) for $\overline{U}$ at $Ca = 0.001$, 0.01, and 0.1, (14) predicts $\hat{r} = 0.9841$, 0.9487, and 0.8269, respectively. If (12) is used for $Ca = 0.001$, the value of $\hat{r}$ would be equal to 0.9866. For a comparison, the computed $r_{z=0} = 0.9872$ (0.9866), 0.9472 (0.9424), and 0.8327 (0.8289) for bubbles of volume $= 3\pi(= 2\pi)$ at $Ca = 0.001$, 0.01 and 0.1 ($Re = 0$), in very good agreement with those corresponding values of $\hat{r}$. As expected, the differences in $\overline{U}$ and $r_{z=0}$ between bubbles of volume $= 3\pi$ and 2π are negligible. However, the values of computed $v_{z=0}$ are 0.9957, 1.0049, and 0.9968 for bubbles of volume $= 3\pi$ as consistent with the uniform annular liquid film theory; but the values of $v_{z=0}$ for bubbles of volume $= 2\pi$ are computed as 0.9285, 0.8938, and 0.9650, indicating considerable nonuniformities of the liquid film free surface at small Ca when bubble volume is not sufficiently large (similar to that found with the buoyancy-driven motion of long bubbles in a tube by Feng, 2008).

Because the uniformity of the liquid film thickness improves at larger Ca, the computational results for bubble of volume $= 2\pi$ are expected to compare well with the theory based on uniform film flow for $Ca \geqslant 1$. For example, at $Ca = 2$ (and $Re = 0$) the computed $\overline{U}$ equals 0.4416 that leads to $\hat{r} = 0.6646$ according to (14), while

the computed $r_{z=0}$ and r_{max} are both 0.6622 (with $v_{z=0} = 0.9908$ and $v_{max} = 0.9911$), respectively (for bubble of volume $= 2\pi$). Again as a comparison, the asymptotic value of $\overline{U}$ suggested by Taylor (1961) based on the measured data at $Ca = 2$ is 0.45 corresponding to $\hat{r} = 0.6708$. If Ca is increased to 10, the computed $\overline{U}$ becomes 0.4084, corresponding to $\hat{r} = 0.6391$ according to (14), in good agreement with the computed $r_{z=0} = r_{max} = 0.6367$ (with $v_{z=0} = v_{max} = 0.9917$). The asymptotic value of $\overline{U}$ obtained by Cox (1962), based on measurements at $Ca > 10$, is 0.40. The values of $\overline{U}$ computed at $Ca = 2$ and 10 (for $Re = 0$) by Giavedoni and Saita (1997) with a semi-infinite long bubble were 0.4410 and 0.4080, respectively.

By virtue of the presently computed results over a large range of Ca values at $Re = 0$, a least-square fitted formula can be obtained in the logistic dose–response form

$$\overline{U} = 1 - \frac{\widetilde{A}}{1 + \widetilde{B}\ Ca^{-\widetilde{C}}}, \tag{15}$$

with $\widetilde{A} = 0.6202$, $\widetilde{B} = 0.1946$, and $\widetilde{C} = 0.7111$. Practically (15) is quite accurate for the entire range of Ca value; for example, it yields $\overline{U} = 0.9774$, 0.8991, 0.6900, 0.4808, and 0.4024, (whereas the corresponding computed values are 0.9753, 0.8967, 0.6945, 0.4754, and 0.4084) for $Ca = 0.001$, 0.01, 0.1, 1, and 10, respectively. At $Ca = 10^{-4}$ (not included in the least-square fitting), it predicts $\overline{U} = 0.9955$, in good agreement with 0.9942 given by (12) and the computed value of 0.9950. As $Ca \to \infty$, the asymptotic value of $\overline{U}$ is predicted by (15) as 0.3798.

3.1. Flow structure and free surface profiles

For effectively displaying the flow field around the entire bubble, results for bubbles of volume $= 2\pi$ are presented herein (such that the aspect ratio of bubble length and tube radius is not excessively large).

3.1.1. Long bubbles (of volume $= 2\pi$) at $Re = 1$

For cases of small Reynolds number, Fig. 2 shows plots of streamlines and shapes of bubbles for $Re = 1$ at $Ca = 0.01$, 0.1, 1, 5, and 10 (which appear to be basically the same as those corresponding to $Re = 0$). As discussed by Taylor (1961) based on a kinematic consideration and later revealed by Martinez and Udell (1989) with a boundary integral analysis and Giavedoni and Saita (1997) with finite-element computations, a recirculating flow ahead of the bubble nose appears in the plots for $Ca = 0.01$ and 0.1 in Fig. 2, with intensity decreasing with increasing Ca and completely disappearing in the plots for $Ca \geqslant 1$. Actually the stagnation ring on the bubble surface is found to collapse into a stagnation point at the bubble nose tip at $Ca \sim 0.610$, as consistent with the finding of Giavedoni and Saita (1997) (at $Ca \sim 0.605$ for $Re = 0$ and semi-infinite bubble). With increasing Ca from 0.610, the recirculating flow detaches from the bubble surface and moves toward upstream forming a second stagnation point on the tube centerline (cf. Taylor, 1961; Giavedoni and Saita, 1997). For example, the second stagnation point is located about 0.622 ahead of the bubble nose tip on the tube centerline when $Ca = 0.690$. The recirculating flow ahead of the bubble nose disappears for $Ca > 0.709$ whereas Giavedoni and Saita, 1997 reported $Ca > 0.690$ (for $Re = 0$ and semi-infinite bubble). Martinez and Udell (1989) reported a recirculation being apparent for $Ca < 0.5$ and disappearing for $Ca \approx 0.7$.

Table 1 shows the computed parameters for bubbles of volume $= 2\pi$ at various values of Ca for $Re = 1$. As expected, the values of $\overline{U}, r_{z=0}, v_{z=0}, r_{max}, v_{max}$, etc. are very close to those corresponding values at $Re = 0$ presented earlier. According to the analysis of Taylor (1961), recirculating flow ahead of the bubble nose is expected to appear when $\overline{U} > 0.5$. Thus, the critical value of Ca for appearance of the recirculating flow must be between 0.5 and 1 because $\overline{U} = 0.5281 > 0.5$ and $0.4774 < 0.5$ at $Ca = 0.5$ and 1. Actually, at $Ca = 0.709$ ($Ca = 0.699$ for $Re = 0$) when the recirculating flow ahead of the bubble nose just disappears, the computed $\overline{U}$ is 0.5003 (0.4995). Hence, computations of bubbles of volume $= 2\pi$ can yield results quite accurately reflecting the general long bubble behavior, especially when $Ca > 0.5$ that the annular liquid film in the middle section becomes quite uniform as indicated by the values of $v_{z=0}$ and v_{max} approaching unity. Little differences can be noticed between the results for $Re = 0$ and 1.

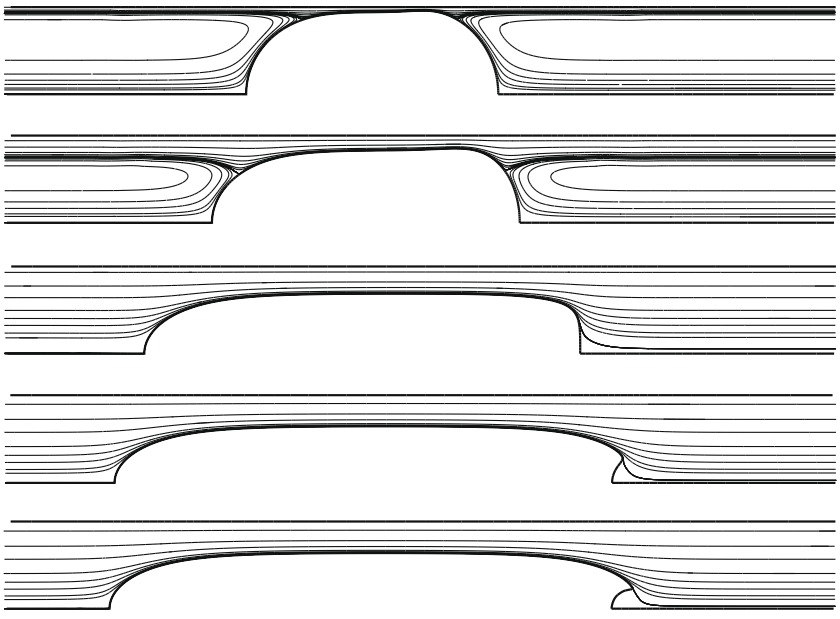

Fig. 2. Streamlines and shapes of bubbles (from $z = -4.5$ to 5) of volume $= 2\pi$ for $Re = 1$ at $Ca = 0.01$, 0.1, 1, 5, and 10. The contour values for streamfunctions shown here are 0, ±0.001, ±0.002, ±0.005, ±0.01, ±0.02, ±0.05, ±0.1, etc. as in Feng (2008).

Table 1
Values of $Ca, \overline{U}, v_{z=0}, r_{z=0}, v_{max}, r_{max}, z_{min}$, and z_{max} for bubbles of volume $= 2\pi$ at $Re = 1$.

Ca	$\overline{U}$	$v_{z=0}$	$r_{z=0}$	v_{max}	r_{max}	z_{min}	z_{max}
0.001	0.9754	0.9284	0.9866	1.4704	0.9901	−1.369	1.345
0.01	0.8967	0.8932	0.9423	1.4091	0.9591	−1.484	1.397
0.1	0.6951	0.9642	0.8291	1.1525	0.8516	−1.877	1.640
0.5	0.5281	0.9871	0.7240	0.9931	0.7252	−2.417	2.093
1	0.4773	0.9893	0.6883	0.9911	0.6888	−2.653	2.330
2	0.4436	0.9905	0.6635	0.9911	0.6637	−2.838	2.558
5	0.4193	0.9913	0.6451	0.9915	0.6451	−2.986	2.804
10	0.4103	0.9916	0.6382	0.9917	0.6382	−3.045	2.929

If the computed values of $\overline{U}$ at $Re = 1$ are fitted to the logistic dose–response curve (15), the values of $\widetilde{A}, \widetilde{B}$, and $\widetilde{C}$ are, respectively, 0.6160, 0.1868, and 0.7213 (which are practically the same as those for $Re = 0$). It yields $\overline{U} = 0.9782$, 0.9003, 0.6894, 0.4810, and 0.4051 for $Ca = 0.001$, 0.01, 0.1, 1, and 10, respectively.

Although the values of $v_{z=0}$ and v_{max} (as well as $r_{z=0}$ and r_{max}) in Table 1 indicate noticeable nonuniformities of the annular liquid film with bubbles of volume $= 2\pi$ for $Ca < 0.5$, the computed value of $\overline{U}$ can still be quite accurate for bubbles of volume $= 2\pi$ when compared with that of volume $= 3\pi$. For example, at $Ca = 0.1$ the computed $v_{z=0} = 0.9968$ for a bubble of volume $= 3\pi$ (much closer to unity than 0.9642 for a bubble of volume $= 2\pi$) with a computed $\overline{U} = 0.69517$ (basically the same as that in Table 1). The uniformity of the annular film for a bubble of volume $= 3\pi$ is verified by examining the degree of $r_{z=0}$ (=0.8331, yielding $r^2_{z=0} = 0.6941$) and $\overline{U}$ satisfying (14).

As discussed by Martinez and Udell (1989), the thickness of the liquid film generally increases with increasing Ca, and a concave deformation (negative curvature) occurs at bubble tail for $Ca > 1$. A similar observation was reported by Goldsmith and Mason (1963), with a reentrant cavity at the trailing meniscus for large Ca. Martinez and Udell (1989) also mentioned difficulties in computing solutions for the trailing meniscus when $Ca > 1$; they computed trailing meniscus solutions up to $Ca = 1.5$ while the leading meniscus solutions were obtained up to $Ca = 10$. The present finite-element code can be used to compute solutions for the entire bubble up to $Ca = 10$ (for $Re \leqslant 1$), beyond which the deformation of the bubble trailing meniscus becomes too severe for the present elliptic meshing scheme to follow.

3.1.2. Long bubbles (of volume $= 2\pi$) at $Re = 10$

At $Re = 10$, Fig. 3 shows very much the same flow structures and bubble shapes as those in Fig. 2, especially for $Ca \leqslant 1$ (as also seen in Table 2). For $Ca > 1$, the fluid inertial effect at $Re = 10$ tends to form a bulge at the bubble tail rim toward the relatively high speed flow (in a shrinking liquid film) along the tube wall (similar to that found by Feng and Basaran (1994)). Although the recirculating flow ahead of the bubble nose disappears for $Ca \geqslant 1$, a weak recirculating eddy can be noticed in the bubble tail due to the flow separation at the tail tip and local concave free surface for $Ca \geqslant 5$ (cf. Figs. 2 and 3). Even at $Ca = 1$, a recirculating eddy exists for $Re = 10$, ending at $z = 2.642$ in the wake. Interestingly, the bubble shape of $Re = 10$ and $Ca = 1$ (or $We = 10$) in Fig. 3 exhibits some similarities to that of buoyancy-driven bubble at $Re = We = 10$ Feng (2008), with about the same thickness of annular liquid film, despite quite different flow structures (as reflected in the streamline distributions).

From the values of $\overline{U}$ in Table 2, it can be recognized that the recirculating flow ahead of bubble nose disappears at Ca slightly less than 1 (for $Re = 10$) based on Taylor's kinematic consideration that leads to the criterion of $\overline{U} = 0.5$.

If the computed values of $\overline{U}$ at $Re = 10$ are fitted to the logistic dose–response curve (15), the values of $\widetilde{A}$, $\widetilde{B}$, and $\widetilde{C}$ are 0.6057, 0.2036, and 0.6939, respectively. It yields $\overline{U} = 0.9763$, 0.8986, 0.6981, 0.4968, and 0.4268 for $Ca = 0.001$, 0.01, 0.1, 1, and 8, respectively.

Unlike the small Reynolds number cases where solutions up to $Ca = 10$ can be obtained, computations become difficult for the cases of $Ca > 8$ at $Re = 10$ due to the cusp formation at the bubble's trailing tip. The similar cusp formation for spherical-cap bubbles moving in an extended liquid was computed by Feng (2007), who found it was consistent with the skirt formation criterion established by Hnat and Buckmaster (1976).

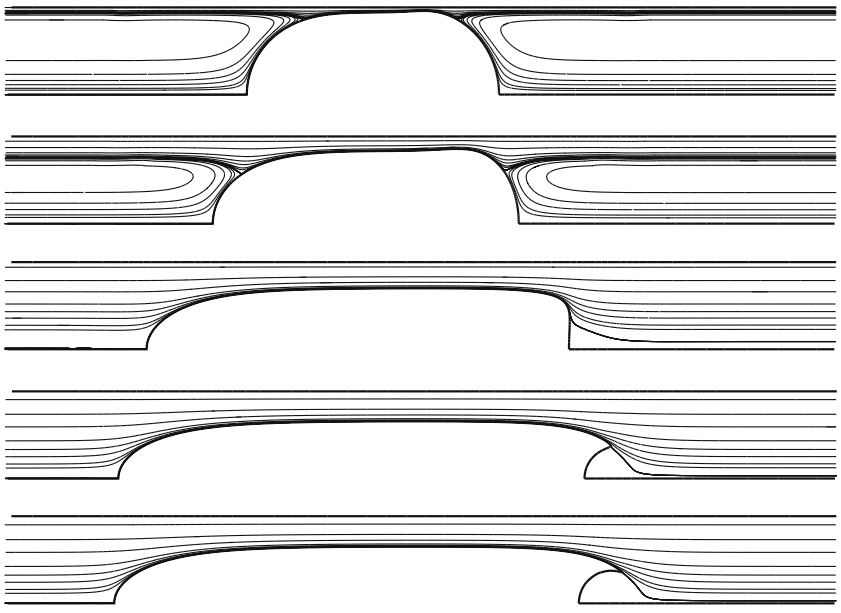

Fig. 3. As Fig. 2 but for $Re = 10$ at $Ca = 0.01$, 0.1, 1, 5, and 8.

Table 2
Values of $Ca, \overline{U}, v_{z=0}, r_{z=0}, v_{max}, r_{max}, z_{min}$, and z_{max} for bubbles of volume $= 2\pi$ at $Re = 10$.

Ca	$\overline{U}$	$v_{z=0}$	$r_{z=0}$	v_{max}	r_{max}	z_{min}	z_{max}
0.001	0.9753	0.9279	0.9866	1.4715	0.9901	−1.369	1.345
0.01	0.8968	0.8875	0.9422	1.4169	0.9594	−1.485	1.397
0.1	0.7016	0.9553	0.8321	1.1671	0.8564	−1.872	1.623
0.5	0.5421	0.9799	0.7324	0.9933	0.7349	−2.397	2.010
1	0.4922	0.9833	0.6978	0.9906	0.6994	−2.629	2.208
2	0.4583	0.9855	0.6734	0.9903	0.6746	−2.811	2.422
5	0.4337	0.9871	0.6551	0.9908	0.6561	−2.958	2.665
8	0.4268	0.9877	0.6501	0.9915	0.6510	−2.999	2.798

3.1.3. Long bubbles (of volume $= 2\pi$) at $Re = 100$

As the Reynolds number is increased to 100, the bubble shapes and flow structures shown in Fig. 4 exhibit noticeable differences when $Ca > 0.1$ compared to those corresponding to the same values of Ca for $Re \leqslant 10$ (as in Figs. 2 and 3). It is difficult to compute a converged solution for $Ca > 2$ at $Re = 100$ (which corresponds to $We = 200$). The bubble shape of $Re = 100$ and $Ca = 0.1$ (or $We = 10$) in Fig. 4 looks quite different from that of a buoyancy-driven bubble (in Feng, 2008), unlike the case of $Re = We = 10$, indicating significant behavioral variations due to the flow structure change. Unlike the bubble nose and the flow structure thereabout that exhibit only insignificant changes with increasing Re (as commented by Giavedoni and Saita, 1997; Heil, 2001, with semi-infinite bubbles), the bubble tail profile and wake structure can be influenced significantly by the value of Re as well as that of Ca. This observation is similar to the buoyancy-driven bubbles presented by Feng (2008). But the shape of recirculating flow in the wake looks quite different from that of the buoyancy-driven bubbles.

Up to $Re = 100$, the results computed here show that all the streamlines ahead of the bubble nose are open, smoothly connecting to the inlet boundary; no sign of the "cat's eye" pattern of closed vortices is present. Actually, the formation of the closed vortex streamline pattern ahead of the bubble nose at finite Re was computationally found by Heil (2001) in a 2D channel, not for the axisymmetric case of round tubes. Thus, whether closed vortices appear ahead of the bubble nose at finite Re might become a signal for differentiating the 2D case and axisymmetric case.[5] Interestingly, in the wake behind the bubble tail, the closed recirculating flow appears at $Re = 100$ for $Ca \geqslant 0.5$ (cf. Fig. 4), with a weak second vortex also appearing further downstream although not shown in the streamline plot of Fig. 4.

The values of $\overline{U}$ in Table 3 for $Ca \leqslant 2$ (and $Re = 100$) are all greater than 0.5. It is then no surprise that all the cases in Fig. 4 show a recirculating flow ahead of the bubble nose. Because at $Ca = 2$ we have $\overline{U} = 0.5061 \sim 0.5$, the stagnation ring almost collapses to a stagnation point at the bubble nose tip and the recirculating flow is confined in a very small region (cf. Fig. 4). Examining the values of $r_{z=0}, r_{max}$ and $v_{z=0}, v_{max}$ in Table 3 suggests that the annular liquid film is not very uniform even at $Ca \geqslant 1$ for bubbles of volume $= 2\pi$. The computed values of $\bar{U}$ with bubbles of volume $= 2\pi$ are nonetheless quite accurate for general long bubbles. For example, the computed values of $\overline{U}$ with bubble volume increasing to 2.5π (for improving the annular liquid film uniformity) are, respectively, 0.5882 (with $r_{max} = 0.7652$ and $v_{max} = 0.9862$) and 0.5401 (with $r_{max} = 0.7285$ and $v_{max} = 0.9679$) for $Ca = 0.5$ and 1.

If the computed values of $\overline{U}$ at $Re = 100$ are fitted to the logistic dose–response curve (15), the values of $\widetilde{A}$, $\widetilde{B}$, and $\widetilde{C}$ become 0.5845, 0.2764, and 0.6176, respectively. It yields $\overline{U} = 0.9718$, 0.8984, 0.7276, 0.5421, and 0.5047 for $Ca = 0.001$, 0.01, 0.1, 1, and 2, respectively.

3.2. Empirical formulas of $\overline{U}$ for long bubbles

With the computed values of $\widetilde{A}(Re)$, $\widetilde{B}(Re)$, and $\widetilde{C}(Re)$ for the logistic dose–response curve (15) of the average liquid flow velocity $\overline{U}$ at $Re = 1$, 10, and 100 ($\log Re = 0$, 1, and 2), quadratic fitting formulas can be obtained as

$$\begin{cases} \widetilde{A}(Re) = -0.0054(\log Re)^2 - 0.0048\log Re + 0.6160 \\ \widetilde{B}(Re) = 0.0280(\log Re)^2 - 0.0112\log Re + 0.1868 \\ \widetilde{C}(Re) = -0.0244(\log Re)^2 - 0.0030\log Re + 0.7213 \end{cases} \quad \text{for } Re \geqslant 1,$$

(with $\log Re$ denoting $\log_{10} Re$) for the general empirical formula

$$\overline{U} = 1 - \frac{\widetilde{A}(Re)}{1 + \widetilde{B}(Re)\ Ca^{-\widetilde{C}(Re)}}. \tag{16}$$

For $Re \leqslant 1$, simple linear fitting formulas

$$\begin{cases} \widetilde{A}(Re) = 0.6202 - 0.0042\,Re \\ \widetilde{B}(Re) = 0.1946 - 0.0078\,Re \\ \widetilde{C}(Re) = 0.7111 + 0.0102\,Re \end{cases} \quad \text{for } Re \leqslant 1,$$

may suffice for practical applications with (16). For example, at $Ca = 0.1$ for $Re = 0.5$, 2, 50, and 200, (16) predicts 0.6897, 0.6836, 0.7143, and 0.7340, in good agreement with the computed $\overline{U}$ of 0.6946, 0.6959, 0.7204, and 0.7294, respectively.

3.3. Long bubbles of different volumes

Similar to that shown by Feng (2008) (as well as many publications cited therein) for the buoyancy-driven motion of long bubbles in tubes, the basic fluid mechanics behavior of long bubbles moving with flowing liquid in a tube appears to be independent of the bubble volume (or bubble length) typically when a bubble's volume-equivalent radius exceeds that of the tube (namely, the bubble volume $>4\pi/3$). As an example, Fig. 5 shows the similarity of the local distribution of pressure contours around the bubble nose and tail for bubbles of different volumes at $Re = 10$ and $Ca = 0.5$. The shapes of as well as pressure distributions around the bubble nose and tail remain invariant, indicating that the pressure drop (i.e., the number of pressure contours) across the bubble is independent of the bubble length. So is the value of $\overline{U} = 0.5421$ for bubbles with volume $\geqslant 4\pi/3$ (at $Re = 10$ and $Ca = 0.5$). This is consistent with the fact that the middle section of uniform annular film flow contributing little hydrodynamic stresses.

Interesting features in hydrodynamic stress distributions can be demonstrated by examining the z-component of traction, or z-traction, T_z, and the net normal traction, or n-traction, T_n, on the bubble surface, where

$$\begin{aligned} T_z &\equiv \boldsymbol{e_z} \cdot (-p_a \boldsymbol{n} - \boldsymbol{n} \cdot \boldsymbol{T}) \\ &= -n_z \left[-(p - p_a) + 2\frac{\partial v_z}{\partial z} \right] - n_r \left(\frac{\partial v_z}{\partial r} + \frac{\partial v_r}{\partial z} \right), \end{aligned} \tag{17}$$

and

$$\begin{aligned} T_n &\equiv p_a + \boldsymbol{nn} : \boldsymbol{T} \\ &= p_a - p + 2\left[n_z n_z \frac{\partial v_z}{\partial z} + n_r n_r \frac{\partial v_r}{\partial r} + n_z n_r \left(\frac{\partial v_z}{\partial r} + \frac{\partial v_r}{\partial z} \right) \right], \end{aligned} \tag{18}$$

with n_z, n_r denoting the z, r-components of the local unit normal vector $\boldsymbol{n}$. The term of constant excess pressure p_a inside the bubble

[5] To verify this fact, the computational code with the same mesh as presented here was also used to compute a few 2D cases at finite Re (as a test), which indeed showed closed vortex streamline pattern ahead of the bubble nose.

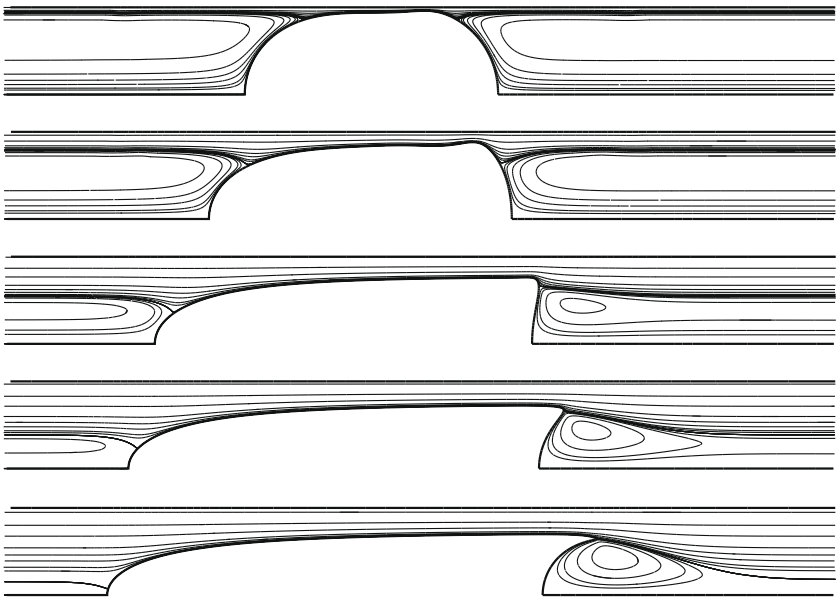

Fig. 4. As Fig. 2 but for $Re = 100$ at $Ca = 0.01$, 0.1, 0.5, 1, and 2.

Table 3
Values of $Ca, \overline{U}$, $v_{z=0}$, $r_{z=0}$, v_{max}, r_{max}, z_{min}, and z_{max} for bubbles of volume $= 2\pi$ at $Re = 100$.

Ca	$\overline{U}$	$v_{z=0}$	$r_{z=0}$	v_{max}	r_{max}	z_{min}	z_{max}
0.001	0.9734	0.9217	0.9864	1.4815	0.9901	−1.370	1.346
0.01	0.8958	0.8261	0.9393	1.4958	0.9610	−1.496	1.399
0.1	0.7287	0.8741	0.8401	1.2625	0.8807	−1.912	1.550
0.5	0.5884	0.8273	0.7354	0.9662	0.7623	−2.530	1.859
1	0.5402	0.8253	0.6980	0.9405	0.7231	−2.827	2.149
2	0.5061	0.8278	0.6713	0.9410	0.6984	−3.070	2.528

does not contribute to the integrated drag force; it only serves as a common reference pressure for comparison purposes. However, p_a in T_n plays a key role in determining the sum of the local principal curvatures (or twice the local mean curvature) of the bubble surface.

Fig. 6 shows the z-traction (a) and n-traction (b) distribution along the bubble surface for bubbles of different volumes at $Re = 10$ and $Ca = 0.5$. The z-traction is negative around the bubble nose whereas positive around the bubble tail while diminishing in the middle section (where $n_z \approx 0$ and $n_r \approx 1$ but $\nabla \boldsymbol{v} \approx 0$), such that the net drag force computed by integrating T_z along the bubble surface as

$$2\pi \int_{S_f} T_z r \, ds = 0, \tag{19}$$

when the buoyancy force is absent. As discussed in Feng (2008) for buoyancy-driven long bubbles, the diminishing value of T_z in the middle section of long bubbles is the key feature to understanding the bubble velocity independence of the bubble length. The value of the n-traction T_n decreases from the tip of bubble nose until reaching the middle section of uniform annular film flow, where $T_n (\approx p_a - p)$ approaches that of $(Ca\, r_{max})^{-1}$. Toward the bubble tail, T_n sharply increases due to the high local curvatures at the rim and then drops down where the surface becomes flat at center of the bubble tail.

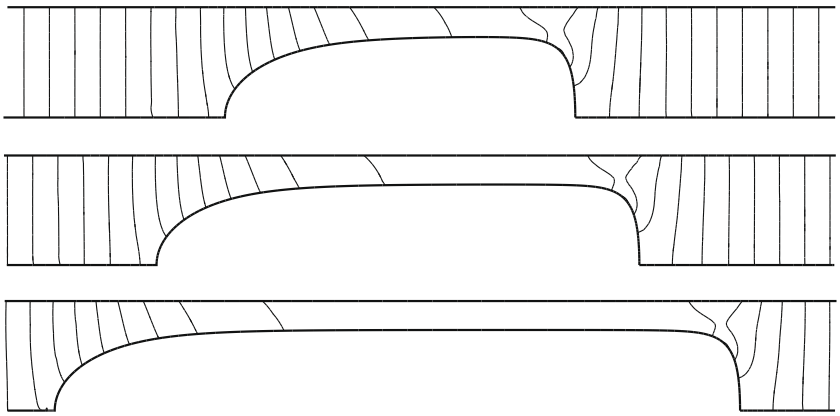

Fig. 5. Pressure contours ($p = p_a \pm 1, p_a \pm 2, p_a \pm 3, \ldots$) for bubbles of volume $= 4\pi/3, 2\pi$, and 3π at $Re = 10$ and $Ca = 0.5$ (from $z = -4$ to 4).

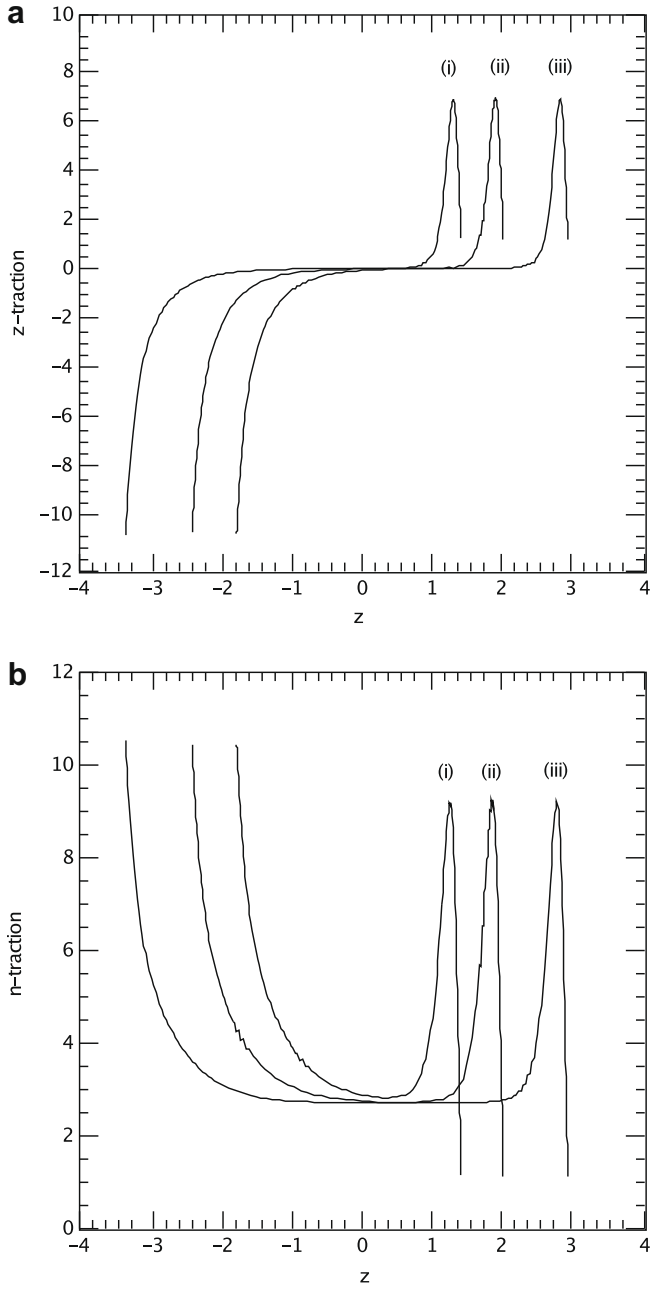

Fig. 6. (a) The z-traction T_z and (b) the n-traction T_n along the bubble surface for bubbles of volume (i) $4\pi/3$, (ii) 2π, (iii) 3π, at $Re = 10$ and $Ca = 0.5$.

4. Conclusions

The Galerkin finite-element method illustrated here is an effective tool for investigating free-surface flow problems such as the present one of long bubbles moving in a tube with a flowing viscous liquid. The behavior of long bubbles for wide ranges of Ca and Re with a variety of shapes can be solved for the steady axisymmetric flow field as well as the free-surface profiles with sufficient accuracy in great details.

When the surface tension effect is relatively weak at $Ca > 1$, the hydrodynamic stresses due to liquid flow around the bubble tend to shape the long bubble surface such that the middle section becomes a cylinder of constant radius with a uniform annular liquid flow adjacent to the tube wall. The annular liquid film thickness generally increases with increasing Ca, but decreases with increasing Re. With increasing the surface tension effect, e.g., when $Ca < 0.1$, the uniformity of annular liquid film deteriorates typically with a bulge forming at the rim of the bubble tail similar to that with the buoyancy-driven long bubbles (Feng, 2008). In units of the bubble moving velocity relative to the tube wall, the average liquid flow velocity $\overline{U}$ is always less than unity indicating that the bubble always moves faster than the average liquid flow, as observed by Fairbrother and Stubbs (1935). The value of $\overline{U}$ generally decreases with increasing Ca, but increases with increasing Re, which is consistent with the trend of the annular liquid film thickness (reported by for the axisymmetric case Giavedoni and Saita, 1997) and the relationship (14).

With a large number of computational results at various values of Ca and Re made available, an empirical formula of $\bar{U}$ as a function of Ca and Re can be obtained in the logistic dose–response form, $\overline{U} = 1 - \widetilde{A}/(1 + \widetilde{B}\,Ca^{-\widetilde{C}})$, with $\widetilde{A}, \widetilde{B}$, and $\widetilde{C}$ being functions of Re. The predicted value of $\overline{U}$ at given Ca and Re is shown to agree with the computed value within a few percents, quite adequate for most practical applications.

Regardless the driving mechanisms, whether it is due to buoyancy (as in Feng, 2008) or liquid flow, the behavior of long bubbles moving in a tube appears independent of the bubble volume (or bubble length). This fact can be explained by examining the stress distributions along the bubble surface, as illustrated in Section 3.3 with plots of z-component and normal tractions for bubbles of different volumes. It is made plain that the uniform annular liquid film flow in bubble's middle section has little influence to fluid mechanic behavior of the bubble.

Acknowledgements

Some of the reviewers' comments helped enhance the presentation contents in this manuscript and are therefore appreciated by the author.

References

Batchelor, G.K., 1967. An Introduction to Fluid Dynamics. Cambridge University Press.
Bretherton, F.P., 1961. The motion of long bubbles in tubes. J. Fluid Mech. 10, 166–188.
Christodoulou, K.N., Scriven, L.E., 1992. Discretization of free surface flows and other moving boundary problems. J. Comput. Phys. 99, 39–55.
Cox, B.G., 1962. On driving a viscous fluid out of a tube. J. Fluid Mech. 14, 81–98.
Fairbrother, F., Stubbs, A.E., 1935. Studies in electroendosmosis. Part VI. The bubble-tube methods of measurement. J. Chem. Soc. 1, 527–529.
Feng, J.Q., 2007. A spherical-cap bubble moving at terminal velocity in a viscous liquid. J. Fluid Mech. 579, 347–371.
Feng, J.Q., 2008. Buoyancy-driven motion of a gas bubble through viscous liquid in a round tube. J. Fluid Mech. 609, 377–410.
Feng, J.Q., Basaran, O.A., 1994. Shear flow over a translationally symmetric cylindrical bubble pinned on a slot in a plane wall. J. Fluid Mech. 275, 351–378.
Giavedoni, M.D., Saita, F.A., 1997. The axisymmetric and plane cases of a gas phase steadily displacing a Newtonian liquid – a simultaneous solution of the governing equations. Phys. Fluids 9, 2420–2428.
Goldsmith, H.L., Mason, S.G., 1963. The flow of suspensions through tubes: II single large bubbles. J. Colloid Sci. 18, 237–261.
Heil, M., 2001. Finite Reynolds number effects in the Bretherton problem. Phys. Fluids 13, 2517–2521.
Hnat, J.-G., Buckmaster, J.D., 1976. Spherical cap bubble and skirt formation. Phys. Fluids 19, 182–194.
Hood, P., 1976. Frontal solution program for unsymmetric matrices. Intl. J. Num. Methods Eng. 10, 379–399 (see ibid. 11, 1055 (1977) for corrigendum).
Kistler, S.F., Scriven, L.E., 1983. Coating flows. In: Pearson, J.R.A., Richardson, S.M. (Eds.), Computational Analysis of Polymer Processing. Applied Science Publishers, London and New York, pp. 243–299.
Martinez, M.J., Udell, K.S., 1989. Boundary integral analysis of the creeping flow of long bubbles in capillaries. Trans. ASME E: J. Appl. Mech. 56, 211–217.
Ortega, J.M., Rheinoldt, W.C., 1970. Iterative Solution of Nonlinear Equations in Several Variables. Academic, London.
Park, C.-W., Homsy, G.M., 1984. Two-phase displacement in Hele–Shaw cells: theory. J. Fluid Mech. 139, 291–308.
Ratulowski, J., Chang, H.-C., 1989. Transport of gas bubbles in capillaries. Phys. Fluids A1, 1642–1655.
Reinelt, D.A., Saffman, P.G., 1985. The penetration of a finger into a viscous fluid in a channel and tube. SIAM J. Sci. Stat. Comput. 6, 542–561.

de Santos, J.M., 1991. Two-phase cocurrent downflow through constricted passages. Ph.D. thesis, University of Minnesota.
Schwartz, L.W., Princen, H.M., Kiss, A.D., 1986. On the motion of bubbles in capillary tubes. J. Fluid Mech. 172, 259–275.
Shen, E.I., Udell, K.S., 1985. A finite-element study of low Reynolds number two-phase flow in cylindrical tubes. ASME J. Appl. Mech. 52, 253–256.
Strang, G., Fix, G.J., 1973. An Analysis of the Finite Element Method. Prentice-Hall.
Taylor, G.I., 1961. Deposition of viscous fluid on the wall of a tube. J. Fluid Mech. 10, 161–165.
Teletzke, G.F., 1983. Thin liquid films: molecular theory and hydrodynamic implications. Ph.D. thesis, University of Minnesota.
Teletzke, G.F., Davis, H.T., Scriven, L.E., 1987. How liquids spread on solids. Chem. Eng. Commun. 55, 41–81.
Teletzke, G.F., Davis, H.T., Scriven, L.E., 1988. Wetting hydrodynamics. Rev. Phys. Appl. 23, 989–1007.